

Extended defects in ZnO: Efficient sinks for point defects

Alexander Azarov,¹ Protima Rauwel,^{1,2} Anders Hallén,³ Edouard Monakhov,¹ and Bengt G. Svensson¹

¹Department of Physics, Centre for Materials Science and Nanotechnology, University of Oslo, P.O. Box 1048 Blindern, N-0316 Oslo, Norway

²Tallinn University of Technology, Tartu College, Puistee 78, 51008 Tartu, Estonia

³Royal Institute of Technology, KTH-ICT, Electrum 229 SE-164 40, Stockholm, Sweden

(Received 27 October 2016; accepted 16 December 2016; published online 10 January 2017)

Dopant-defect reactions dominate the defect formation in mono-crystalline ZnO samples implanted with Ag and B ions. This is in contrast to most other ion species studied and results in an enhanced concentration of extended defects, such as stacking faults and defect clusters. Using a combination of B and Ag implants and diffusion of residual Li atoms as a tracer, we demonstrate that extended defects in ZnO act as efficient traps for highly mobile Zn interstitials. The results imply that dynamic annealing involving interaction of point defects with extended ones can play a key role in the disorder saturation observed for ZnO and other radiation-hard semiconductors implanted with high doses. Published by AIP Publishing. [<http://dx.doi.org/10.1063/1.4973463>]

For the past decade, research on ZnO materials has been stimulated by potential applications for next generation of opto-electronic devices working in the short (ultra-violet) wavelength region.¹ However, a true realization of bipolar ZnO-based devices is hindered by poor understanding of intrinsic point and extended structural defects as well as of defect complexes involving impurities. For instance, the well-known doping asymmetry issue,² where ZnO is found to be readily doped n-type only, can partly be attributed to (i) compensation of acceptor dopants by prevalent intrinsic defects (hole killers) such as zinc interstitials (Zn_i) and oxygen vacancies (V_O), (ii) their interaction with residual impurities, and/or (iii) self-compensation effects.^{2,3}

The situation becomes even more challenging for doping by ion implantation where the various types of generated defects accumulate, including clusters and extended defects such as stacking faults and dislocation loops.^{4,5} In contrast to more common semiconductors such as Si and GaAs, the defect accumulation in implanted ZnO exhibits a somewhat unusual behavior. In particular, it is known that even at cryogenic temperatures ZnO cannot be rendered amorphous due to ballistic processes only.^{6,7} A similar strong radiation resistance has also been observed for other non-metallic materials like CdTe, MgO,⁸ and cubic zirconia crystals;⁹ however, its reason is still under debate. Already in 1975, it was suggested that the efficiency of dynamic defect annealing and, therefore, the resistance to amorphization is related to the degree of ionicity of the chemical bonds of the materials.¹⁰ More recently, Trachenko *et al.*¹¹ tried to quantify the resistance to amorphization of complex materials based on a competition between the short-range covalent and long-range ionic forces. Despite that this approach adequately predicts the radiation resistance for a wide range of materials, the multi-stage character of defect accumulation with implantation dose typically observed in semiconductors with a high degree of dynamic annealing^{7,8} is out of the scope of the model. However, it appears indisputable that the disorder accumulation in non-amorphizable materials hinges on the formation and evolution of different type defects,⁸ so the

interaction of point defects with larger ones has a critical role.¹² In its turn, the implanted element itself and its diffusivity can dramatically affect the thermal defect evolution.^{13–15}

In the present study, we address the ion-induced defect microstructure, interaction of extended defects with mobile point defects, and crystal recovery during post-implantation annealing of mono-crystalline ZnO samples. Correlating diffusion and structural data, it is demonstrated that Ag implantation results in enhanced formation of extended defects which act as efficient sinks for highly mobile Zn interstitials. The present results have technological implications for defect engineering, isolation, and selective area doping of ZnO-based devices.

Hydrothermally (HT) grown wurtzite ZnO single crystals obtained from Mineral, Ltd., were implanted at room temperature with 500 keV Ag ions to a dose of $5 \times 10^{15} \text{ cm}^{-2}$ using 1 MV tandem accelerator (NEC, model 3SDH-2). The dose uniformity over the sample was $\leq 2\%$, and the implantations were carried out either in the [0001] aligned direction or at 7° off-axis in order to enhance and reduce channeling, respectively. In addition, selected Ag on-axis implanted samples as well as virgin ones were off-axis implanted with 35 keV B ions to a dose of $3 \times 10^{15} \text{ cm}^{-2}$. The energy of the B ions was selected such that a more shallow B profile was formed compared to that for Ag; the estimated projected range (R_p) of the B ions is $\sim 90 \text{ nm}$, which is about half of that of the Ag ions.¹⁶ After implantation, the samples were isochronally annealed for 30 min in air at temperatures between 500 and 1150°C . The structural quality of the samples was analyzed by Rutherford backscattering/channeling spectrometry (RBS/C) with $1.6 \text{ MeV } ^4\text{He}^+$ ions incident along the [0001] direction and backscattered into a detector positioned at 170° relative to the incident beam direction. The analysis of the raw RBS/C spectra was done using the DICADA code¹⁷ in order to deduce an effective number of scattering centers, referred to below as “relative disorder.” Selected samples were studied by transmission electron microscopy (TEM) to characterize the defect microstructure. The specimens for TEM were prepared by mechanical

thinning followed by 4 keV Ar-ion milling for approximately 30 min at room temperature. The TEM observations were carried out along the $[11\bar{2}0]$ zone axis using a JEM2010F microscope operating at 200 kV and disposing a point to point resolution of 1.9 Å.

The Ag as well as Li (which is one of the main residual impurities in HT-ZnO and homogeneously distributed at a level of $\sim 3\text{--}5 \times 10^{17} \text{ cm}^{-3}$) concentration versus depth profiles were measured by secondary ion mass spectrometry (SIMS) using a Cameca IMS 7f microanalyzer with 10 keV O_2^+ ions as the primary beam. The intensity-concentration calibration was performed using the Ag as-implanted sample and a Li as-implanted standard sample as references. The conversion from sputtering time to sample depth was performed by measurement of the crater depth utilizing a Dektak 8 stylus profilometer and assuming a constant erosion rate with time.

Comparison of RBS/C spectra for the samples implanted at channeling and off-axis directions is shown in Fig. 1. Even for off-axis implantation, the RBS/C spectrum exhibits an enhanced yield beyond the bulk damage peak located at depths around 180–200 nm. It has been demonstrated previously¹⁸ that such an increased dechanneling yield implies the formation of correlated extended defect structures in the implanted region which do not contribute to direct ion back-scattering. Note that the observed damage behavior is different from that of other implanted species, including both light^{13,15} and heavy ones,^{5,15,19,20} where the ion-induced disorder after high doses is characterized by a peak in the RBS/C spectra, located around (or slightly deeper than) R_p . In contrast to the off-axis implant, the RBS/C spectrum for the on-axis implanted sample does not show a well defined damage peak. Instead, it displays a considerably enhanced yield deeper than R_p (marked by the arrow),²¹ while the spectrum shallower than R_p is close to that of the unimplanted (virgin) sample. The results show that the concentration of extended defects has a weak dependence on the off-axis versus on-axis implantation direction, in contrast to that

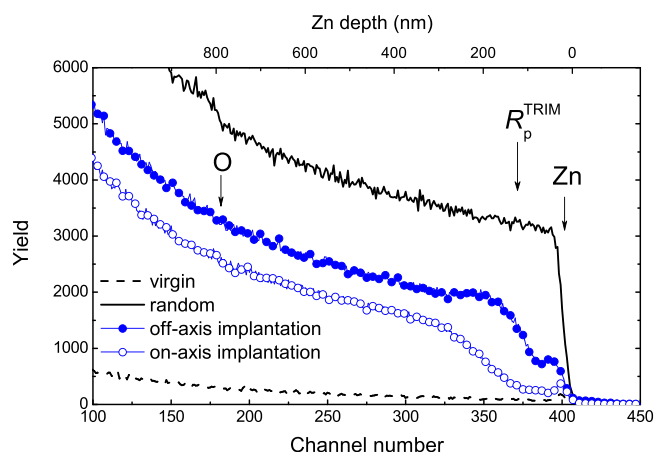


FIG. 1. RBS/C spectra of ZnO samples implanted with 500 keV Ag^+ ions to a dose of $5 \times 10^{15} \text{ cm}^{-2}$ in a channeling (open symbols) and off-axis (closed symbols) directions as indicated in the legend. The TRIM predicted R_p of the implanted ions in correlation with the Zn depth scale as well as the surface positions of Zn and O atoms are shown by the arrows. The channeling and random spectra of a virgin sample are also depicted for comparison (dashed and solid lines).

of the defects forming the bulk peak and consisting of uncorrelated imperfections such as point-defects and clusters thereof. Hence, the formation of extended defects appears to be closely linked to the presence of Ag atoms.

The existence of extended defects is also evidenced by the high resolution TEM (HRTEM) results carried out near the sample surface for an on-axis Ag implanted sample. A Fast Fourier Transform (FFT) selecting the (0002) reflection was performed followed by inversion of the FFT. This allows us to obtain only lattice spacing corresponding to the (0002) reflection harboring possible stacking faults. The Fourier filtered image in Fig. 2(a) (see also [supplementary materials](#)) reveals a high density of planar defects consisting of three types of defect structures typical for a wurtzite crystal structure.²² In particular, the encircled defect numbered 1 corresponds to two opposite sign dislocations; defect number 2 is faulting on the $(\bar{1}10\bar{1})$ plane due to point defects which lead to pyramidal dislocation loops, while defect 3 is an extra (0001) plane arising from interstitial dislocation loops. Note that basal stacking faults are the most common ones in Wurtzite materials, and Wang *et al.*²² have suggested that interstitials condense on the basal plane while vacancies condense on the pyramidal planes. A defect microstructure with a high density of stacking faults was also observed in Ag-doped ZnO nanostructures grown by metal-organic chemical vapor deposition.²³ Interestingly, a correlation between p-type conductivity of ZnO and the presence of stacking faults has been pointed out by several groups;^{24,25} Thonke *et al.*²⁶ suggested that the stacking faults rather than the introduced impurities were responsible for the formation of shallow acceptor states, which may explain some of the contradictory results on p-type doping of ZnO. Hence, the defect microstructure in Ag implanted samples may be beneficial if a controllable defect-induced doping can be accomplished.

At present, the exact role of the Ag atoms in extended defect formation is not clear, but it can be suggested that agglomeration of the Ag atoms occurs. Indeed, despite that it is impossible to identify the atomic configuration(s) of the Ag atoms based on the obtained results, the large difference in ionic radii between Ag^+ and Zn^{2+} ions and a relatively low Ag solid solubility provide arguments for efficient clustering, especially at high Ag concentrations. Further, high probability for Ag agglomeration, where formation of the

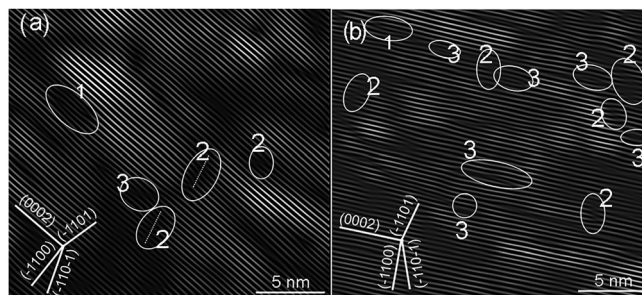


FIG. 2. Fourier filtered (0002) diffraction HRTEM images of ZnO (0001) samples implanted on-axis with 500 keV Ag ions to $5 \times 10^{15} \text{ cm}^{-2}$ before (a) and after annealing (b). The images have been taken near the surface part of the damaged region along the $[11\bar{2}0]$ zone axis with different planes indicated. The various defects are numbered: 1 corresponds to two opposite sign dislocations; 2—pyramidal dislocation loops; and defect 3 is an extra (0001) plane.

wurtzite AgO phase can occur, has also been predicted by results from first principle calculations.²⁷ Such inclusions induce local strain in the crystal and promote generation of stacking faults. The latter, in their turn, can act as sinks for migrating point defects and suppress clustering thereof (see also discussion below).

Fig. 3 illustrates the damage evolution during isochronal annealing of on-axis Ag implanted samples, as deduced from RBS/C spectra, in comparison with that for off-axis Cd implanted ones. The extended defects in the Ag samples are stable up to 600 °C, and at higher temperature, a gradual recovery of the crystal structure takes place. This evolution with temperature differs substantially from that for other heavy elements where the annealing displays a distinct two step behavior, as shown in Fig. 3 for 250 keV Cd ions (data are taken from Ref. 15). As demonstrated in Ref. 15, the first stage occurs at ≤ 500 °C and is associated with the disappearance of uncorrelated defect structures. The second one is attributed to more gradual annealing of extended defects at higher temperatures and, therefore, the latter process appears to dominate in the Ag implanted samples. The evolution of the defect microstructure with annealing is exemplified by Figs. 2(b) showing Fourier filtered HRTEM image obtained with the (0002) reflection after the heat treatment at 800 °C. Fig. 2(b) unveils that the basal plane stacking faults are shorter than in the as-implanted sample and also more frequent. In contrast, the pyramidal plane dislocation loops remain about the same as prior to annealing.

It should be noted that, despite a complex interaction between the Ag atoms and the implantation-induced defects during annealing,^{28,29} no direct correlation is found between the annealing of extended defects and out-diffusion of implanted atoms. Indeed, as illustrated by Fig. 3, a substantial loss of Ag atoms takes place in a relatively narrow temperature range (800–900 °C), but with no corresponding improvement in crystallinity. Furthermore, almost complete crystal recovery occurs after the 1100 °C anneal, while $\sim 25\%$ of the implanted Ag atoms still remains. In contrast, for ion species such as F¹³ and rare earth elements,^{30–32} the crystal recovery, associated with annealing

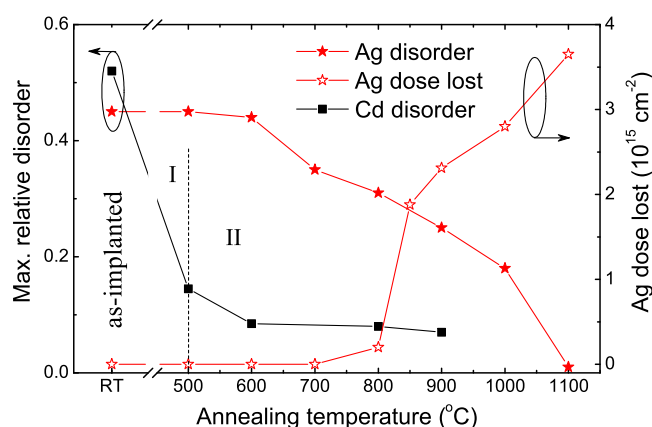


FIG. 3. Relative disorder on the Zn-sublattice as deduced from RBS/C spectra at the maximum of the damage profiles (left-hand scale) in Ag and Cd (Ref. 15) implanted samples and the fraction of lost Ag dose in the implanted region (right-hand scale) as a function of annealing temperature.

of uncorrelated defect structures, is accompanied by a strong out-diffusion of the implanted atoms. The relatively high annealing temperatures of the Ag-induced defects are also consistent with the empirical rule that temperatures of $\sim 2/3$ of the melting point (in K) are needed for complete removal of extended defects in semiconductors,³³ giving ~ 1200 °C for ZnO.

In order to reveal an interaction of mobile point defects with extended defects we use residual Li atoms as a tracer. It has recently been demonstrated³⁴ that the evolution of self-interstitials (Zn_i and O_i) in ZnO can be traced by monitoring the Li concentration versus depth profiles. For example, the formation of a Li depleted region beyond R_p is typical for samples implanted with Zn-substituting elements and subsequently annealed between 600 and 800 °C. This is ascribed to fast moving interstitial Li (Li_i) formed via the kick-out mechanism ($Zn_i + Li_{Zn} \rightarrow Zn_{Zn} + Li_i$). In its turn, the Zn_i flux is determined by the annealing kinetics of the implantation-induced defects. Previously, we demonstrated that annealing of B implanted samples leads to an efficient injection of Zn_i 's in a relatively wide temperature range.¹⁵ Therefore, the B damaged region in the co-implanted samples can be considered as a source of Zn_i 's located between the surface and Ag peak.

Fig. 4 shows the Li concentration versus depth profiles in the Ag, B, and Ag+B implanted samples after 800 °C anneals. In contrast to Ag demonstrating a relatively modest Li redistribution, a wide Li depletion region reaching $\sim 25 \mu m$ forms in the B implanted sample.³⁵ This difference in the Li behavior for Ag and B ions is primarily attributed to different types of predominant defects in the two cases and, therefore, different kinetics of their annealing. Intriguingly enough, for Ag+B, the Li depletion exhibits not an additive effect, i.e., the amount of Li depleted in the co-implanted sample is not the sum of that in the B and Ag implanted ones. Instead, the width of the Li depletion in the co-doped sample is smaller by a factor of ~ 2.5 compared to that in the B implanted sample only. The observed Li behavior is attributed to trapping of Zn_i 's released from the B-induced defect structures by the Ag-induced extended defects and/or direct interaction of Zn_i 's with the Ag atoms. In order to reveal the importance of the latter mechanism,

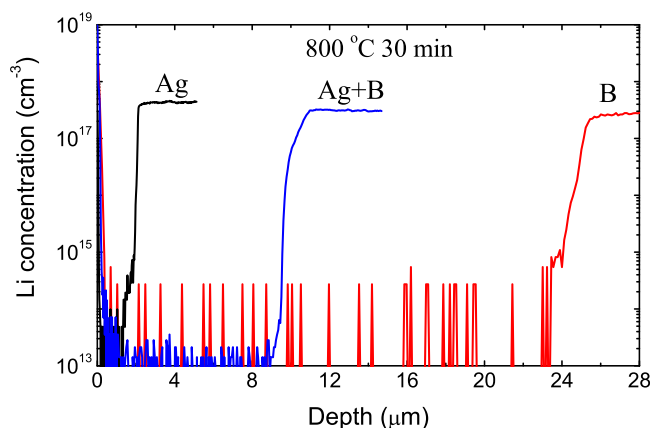


FIG. 4. Li concentration vs. depth profiles as measured by SIMS in Ag and B implanted as well as Ag+B co-implanted samples after 800 °C anneals.

the Ag behavior has been monitored in addition to the Li redistribution in the Ag and B+Ag implanted samples after annealing.

Fig. 5 shows the Ag and Li concentration versus depth profiles in Ag implanted and co-implanted samples after 750 and 800 °C annealing. The Ag atoms display only a minor redistribution below 800 °C, while an unexpected pile-up occurs at $\sim 2 \mu\text{m}$ after 800 °C in the Ag implanted sample. Concurrently, Li exhibits a depletion and the position of the Ag pile-up corresponds closely to the width of the Li depleted region. The Ag pile-up can be attributed to a competition between Zn and Ag atoms to occupy Zn substitutional sites, where Zn_{Zn} has a lower total energy as compared to that for Ag_{Zn} and Ag_i redistributes to the end of the region exposed to Zn_i 's, as corroborated by the Li profiles.³⁶ This effect is also pronounced in the B+Ag co-implanted samples, where the larger Zn_i flux results in a Ag pile-up at $\sim 10\text{--}12 \mu\text{m}$ (see Fig. 5). Therefore, the formation of stable and immobile Ag complexes by trapping of Zn_i 's is not likely but rather that Zn_i 's mediate Ag diffusion.

Accordingly, the reduced Li depletion in the co-implanted samples, Fig. 4, is primarily attributed to trapping of the Zn_i 's by the extended defects. The trapping rate can be roughly estimated by comparing the amount of Li removed in the B and B+Ag samples and the difference gives a value of $\sim 3 \times 10^{11} \text{ at./}(\text{cm}^2 \text{ s})$ at 800 °C assuming a constant Zn_i flux during the duration of 30 min. However, it has been demonstrated that the Li depletion is highly nonlinear with annealing time and substantial Zn_i injection and Li redistribution occurs in the first 10–20 s.³⁷ Therefore, the actual Zn_i trapping rate can be up to 2 orders higher than the estimated value and be in the range of $10^{13} \text{ at./}(\text{cm}^2 \text{ s})$. Obviously, such an efficient interaction of extended defects with Zn_i 's will affect the defect accumulation under ion irradiation/annealings and, therefore, play a crucial role for the disorder saturation in ZnO (and other radiation resistant materials) at high doses.

Unlike most other elements, implantation by Ag induces disorder in ZnO exhibiting an enhanced concentration of planar defects such as stacking faults. The formation of the extended defects has a weak dependence on the ion-beam alignment with respect to the crystal structure and on-axis

implantation reduces only the concentration of uncorrelated defect structures. Heat treatment leads to a gradual annealing of these extended defects primarily due to a decrease of the stacking faults length, and complete crystal recovery occurs at temperatures $\geq 1100 \text{ °C}$. Using Li as a tracer for the point defect interaction, it is argued that the extended defects are efficient traps for highly mobile Zn_i 's and play a crucial role for the saturation in disorder accruing at high doses. Further, the results also imply that a device processing strategy involving co-implantation can be used to control defect interaction with implications for selective area doping and device isolation in ZnO.

See [supplementary material](#) for the TEM and HRTEM images of ZnO sample as-implanted on-axis with 500 keV Ag^+ ions to a dose of $5 \times 10^{15} \text{ cm}^{-2}$.

This work was performed within The Norwegian Research Centre for Solar Cell Technology (project number 460976), a Centre for Environment-friendly Energy Research cosponsored by the Norwegian Research Council and research and industry partners in Norway.

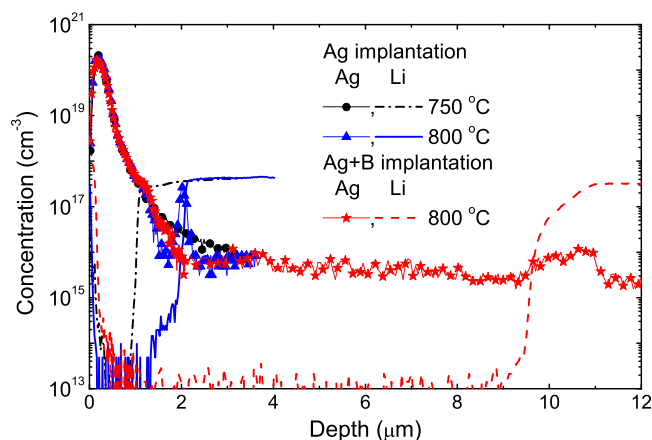


FIG. 5. Ag (symbols) and Li (lines) concentration vs. depth profiles as measured by SIMS in ZnO samples implanted on-axis with Ag ions and co-implanted with B+Ag ions after anneals as indicated in the legend.

- ¹Ü. Özgür, Y. I. Alivov, C. Liu, A. Teke, M. A. Reshchikov, S. Doğan, V. Avrutin, S.-J. Cho, and H. Morkoç, *J. Appl. Phys.* **98**, 041301 (2005).
- ²C. H. Park, S. B. Zhang, and S.-H. Wei, *Phys. Rev. B* **66**, 073202 (2002).
- ³S. B. Zhang, *J. Phys.: Condens. Matter*, **14**, R881 (2002).
- ⁴G. Perillat-Merceroz, P. Gergaud, P. Marotel, S. Brochen, P.-H. Jouneau, and G. Feuillet, *J. Appl. Phys.* **109**, 023513 (2011).
- ⁵S. O. Kucheyev, J. S. Williams, C. Jagadish, J. Zou, C. Evans, A. J. Nelson, and A. V. Hamza, *Phys. Rev. B* **67**, 094115 (2003).
- ⁶K. Lorenz, E. Alves, E. Wendler, O. Bilani, W. Wesch, and M. Hayes, *Appl. Phys. Lett.* **87**, 191904 (2005).
- ⁷A. Yu. Azarov, E. Wendler, A. Yu. Kuznetsov, and B. G. Svensson, *Appl. Phys. Lett.* **104**, 052101 (2014).
- ⁸W. Wesch, E. Wendler, and C. S. Schnohr, *Nucl. Instrum. Methods Phys. Res., B* **277**, 58 (2012).
- ⁹A. Debelle, J. Channagiri, L. Thomé, B. Décamps, A. Boule, S. Moll, F. Garrido, M. Behar, and J. Jagielski, *J. Appl. Phys.* **115**, 183504 (2014).
- ¹⁰H. M. Naguib and R. Kelly, *Radiat. Eff.* **25**, 1 (1975).
- ¹¹K. Trachenko, J. M. Pruneda, E. Artacho, and M. T. Dove, *Phys. Rev. B* **71**, 184104 (2005).
- ¹²A. Yu. Azarov, A. I. Titov, and S. O. Kucheyev, *J. Appl. Phys.* **108**, 033505 (2010).
- ¹³A. Yu. Azarov, B. G. Svensson, and A. Yu. Kuznetsov, *Appl. Phys. Lett.* **101**, 222109 (2012).
- ¹⁴Z. Q. Chen, M. Maekawa, A. Kawasuso, S. Sakai, and H. Naramoto, *J. Appl. Phys.* **99**, 093507 (2006).
- ¹⁵A. Yu. Azarov, A. Hallén, X. L. Du, P. Rauwel, A. Yu. Kuznetsov, and B. G. Svensson, *J. Appl. Phys.* **115**, 073512 (2014).
- ¹⁶J. F. Ziegler, J. P. Biersack, and U. Littmark, *The Stopping and Range of Ions in Solids* (Pergamon, Oxford, 1985), Vol. 1, p. 109.
- ¹⁷K. Gärtner, *Nucl. Instrum. Methods Phys. Res., B* **227**, 522 (2005).
- ¹⁸E. Wendler, O. Bilani, K. Gärtner, W. Wesch, M. Hayes, F. D. Aurret, K. Lorenz, and E. Alves, *Nucl. Instrum. Methods Phys. Res., B* **267**, 2708 (2009).
- ¹⁹A. Yu. Azarov, A. Hallén, B. G. Svensson, and A. Yu. Kuznetsov, *J. Phys. D: Appl. Phys.* **45**, 235304 (2012).
- ²⁰E. Sonder, R. A. Zhur, and R. E. Valiga, *J. Appl. Phys.* **64**, 1140 (1988).
- ²¹It should be noted that the measured Ag peak by SIMS in the on-axis implanted sample is located $\sim 50\%$ deeper as compared to simulated one by the TRIM code [16] that is attributed to channeling effects.
- ²²C. M. Wang, W. Jiang, W. J. Weber, and L. E. Thomas, *J. Mater. Res.* **17**, 2945 (2002).
- ²³V. Khranovskyy, I. Tsiaoussis, M. Eriksson, and R. Yakimova, *Phys. Status Solidi A* **211**, 2109 (2014).
- ²⁴M. A. Myers, M. T. Myers, M. J. General, J. H. Lee, L. Shao, and H. Wang, *Appl. Phys. Lett.* **101**, 112101 (2012).
- ²⁵W. Guo, A. Allenic, Y. B. Chen, X. Q. Pan, Y. Che, Z. D. Hu, and B. Liu, *Appl. Phys. Lett.* **90**, 242108 (2007).

- ²⁶K. Thonke, M. Schirra, R. Schneider, A. Reiser, G. M. Prinz, M. Feneberg, R. Sauer, J. Biskupek, and U. Kaiser, *Phys. Status Solidi B* **247**, 1464 (2010).
- ²⁷O. Volnianska, P. Boguslawski, J. Kaczkowski, P. Jakubas, A. Jezierski, and E. Kaminska, *Phys. Rev. B* **80**, 245212 (2009).
- ²⁸A. Azarov, L. Vines, P. Rauwel, E. Monakhov, and B. G. Svensson, *J. Appl. Phys.* **119**, 185705 (2016).
- ²⁹F. Yaqoob and M. Huang, *J. Appl. Phys.* **120**, 045101 (2016).
- ³⁰E. Rita, E. Alves, U. Wahl, J. G. Correia, T. Monteiro, M. J. Soares, A. Neves, and M. Peres, *Nucl. Instrum. Methods Phys. Res. B* **242**, 580 (2006).
- ³¹A. Azarov, A. Galeckas, A. Hallén, A. Kuznetsov, E. Monakhov, and B. G. Svensson, *J. Appl. Phys.* **118**, 125703 (2015).
- ³²P. P. Murmu, R. J. Mendelsberg, J. Kennedy, D. A. Carder, B. J. Ruck, A. Markwitz, R. J. Reeves, P. Malar, and T. Osipowicz, *J. Appl. Phys.* **110**, 033534 (2011).
- ³³J. S. Williams, *Mater. Sci. Eng. A* **253**, 8 (1998).
- ³⁴A. Yu. Azarov, P. T. Neuvonen, K. E. Knutsen, L. Vines, B. G. Svensson, and A. Yu. Kuznetsov, *Phys. Rev. Lett.* **110**, 175503 (2013).
- ³⁵Note that different noise values for the Li concentrations in the bottom of the depleted regions for the B versus the Ag(Ag+B) implanted samples is due to slightly different settings of the SIMS instrument.
- ³⁶G.-Y. Huang, C.-Y. Wang, and J.-T. Wang, *J. Phys: Condens. Matter.* **21**, 345802 (2009).
- ³⁷P. T. Neuvonen, L. Vines, B. G. Svensson, and A. Yu. Kuznetsov, *Phys. Rev. Lett.* **110**, 015501 (2013).